Retrieving intracycle interference in angle-resolved laser-assisted photoemission from argon

Retrieving intracycle interference in angle-resolved laser-assisted photoemission from argon

Johan Hummert,[1] Markus Kubin,[1] Sebastián D. López,[2] Johanna I. Fuks,[3] Felipe Morales,[1] Marc J. J. Vrakking,[1] Oleg Kornilov *,[1] and Diego G. Arbó †[2]

[1] *Max-Born-Institute, Max-Born-Straße 2A, 12489 Berlin, Germany*
[2] *Institute for Astronomy and Space Physics IAFE (UBA-Conicet), C1428ZAA, Buenos Aires, Argentina*
[3] *Departamento de Física, Facultad de Ciencias Exactas y Naturales, Universidad de Buenos Aires, Argentina*

(Dated: April 20, 2020)

We report on a combined experimental and theoretical study of XUV ionization of atomic argon in the presence of a near-infrared (NIR) laser field. Using a table-top source of wavelength-selected femtosecond XUV pulses in combination with a velocity map imaging spectrometer we record angle- and energy-resolved photoelectron distributions and simulate the experimental data by solving the time-dependent Schrödinger equation *ab initio*. In order to compare with the experimental data we average the calculated energy-angle probability distributions over the experimental focal volume for different values of the magnetic quantum number of the photoelectron. This averaging procedure washes out the intracycle interference pattern, which would otherwise be observed in the form of angular modulations of the photoelectron spectra. We recover these modulations experimentally and in the simulations by evaluating the difference between two averaged distributions that are obtained for slightly different NIR laser field intensities.

PACS numbers: 32.80.Rm, 32.80.Fb, 03.65.Sq

I. INTRODUCTION

The generation of XUV pulses via high-order harmonic generation (HHG) opens new routes for time-resolved spectroscopy with unprecedented time resolution. In combination with near-infrared or visible (NIR/vis) laser light, such XUV pulses allow the control of electron motion on ultrashort timescales. The most readily observed effect in such experiments is the laser-assisted photoelectric effect (LAPE), where the NIR/vis light controls the trajectories of free electrons created by the short XUV pulse [1–3]. For XUV pulses longer than the NIR laser cycle, the photoelectron spectrum consists of an XUV-only ionization peak and a sequence of adjacent equally spaced sidebands (SB) with a separation equal to the NIR/vis photon energy [1, 2]. Sidebands, which reflect the interference of electron trajectories born in different cycles of the control field (i.e., intercycle interference), have been observed in laser-assisted ionization of gases, liquids and solids [4–11]. Their study can be used to extract information on the XUV pulse duration, the NIR laser intensity, and the time delay between the two pulses [12–14].

For sufficiently high intensity of the NIR/vis pulse another class of features appears in the photoelectron spectra, which stems from intracycle interferences. For linearly polarized pulses modulations of the photoelectron angular distributions that are commonly referred to as the "gross structure" are expected [15–17]. Until now this effect has not been observed in HHG-based experiments, but it has been reported for the ionization of Ne and other noble gases at free-electron laser facilities (FEL), along with a comparison to calculations [10, 11, 18].

There are a number of approaches to describe the laser-assisted photoelectric effect theoretically [12–16, 19]. For example, in Refs. [20, 21] numerical solution of the time-dependent Schrödinger Equation (TDSE) was used relying on the single-active-electron (SAE) approximation. The well-known soft-photon approximation [19, 22] and the theory of Bivona *et al* [17] describe some general features in experiments [8, 10, 23–26]. Furthermore, improvements to the soft-photon approximation based on the strong field approximation (SFA) and the Coulomb-Volkov approximation were developed by several authors [15–17] and in our own previous theoretical work [27–29] in order to gain physical insight into the dynamics of photoionization in the presence of an oscillating laser field.

In this paper we use the theoretical tools developed in Refs. [27–29] to analyze experiments where energy and angle-resolved photoelectron spectra were measured utilizing a laboratory-based XUV source. In our experiment, XUV pulses generated by HHG are filtered by a time-delay-compensating monochromator [30] and combined with a replica of the femtosecond NIR pulse in order to induce two-color XUV-NIR ionization of argon. Owing to the precise synchronization of the XUV and NIR laser pulses this experimental scheme does not suffer from the time jitter experienced in FEL-based experiments [7].

The small bandwidth of the XUV pulses filtered by the monochromator allows studying photoelectron sidebands in the absence of interference effects from adjacent harmonic orders [31, 32]. This setup is hence an ideal tool for the investigation of sideband generation and the re-

* kornilov@mbi-berlin.de
† diego@iafe.uba.ar

lated physics of strong-field and multiphoton nonlinear effects which occur in LAPE . In combination with a velocity map imaging spectrometer [33], angular distributions are measured, which provide detailed information on the photoionization process, such as the partial wave character of the emitted photoelectrons and relative ionization phases. In the experiments the intensity of the NIR field varies across the laser focus, leading to a "washing out" of the gross structure, which is very sensitive to the field strength [34]. We compare the experimental results with theoretical calculations that solve the TDSE fully *ab initio*. To recover the intracycle interference that results in the gross structure we implement a scheme for averaging the calculated spectra over the focal volume.

The paper is organized as follows. In Sec. II we describe the experimental setup to measure velocity-map images for ionization of argon by narrowband XUV pulses in the presence of a NIR laser pulse and present the experimental results. In Sec. III we describe the theoretical methods for computing angle-resolved photoelectron spectra and the calculation method to simulate the averaging over the focal volume, which results in a washing out of the intracycle interference. We show that, under our experimental conditions, the subtraction of two measured/calculated distributions obtained for slightly different peak intensities leads to a recovery of the intracycle interference pattern. In Sec. IV, we present the theoretical results obtained by solving the TDSE, compare them with the measurements, and discuss the details of the sideband modulation produced by the intracycle interference. Concluding remarks are presented in Sec. V. We employ atomic units throughout this work except when stated otherwise.

II. EXPERIMENTAL SETUP AND RESULTS

The experiments are carried out at an XUV time-delay-compensating monochromator beamline described in detail elsewhere [30, 35]. In short, 1.5 mJ pulses with a duration of 25 fs from a 1 kHz Ti:Sa laser system are used to generate high-order harmonics in argon. The XUV spectrum consists of a sequence of odd harmonics of the driving NIR laser field (795 nm) spanning a photon energy range from 10 to 50 eV. The XUV beam is guided through a time-delay-compensating monochromator and one harmonic is selected. Thanks to the compensation scheme the XUV pulse retains its pulse duration, which is therefore shorter or equal to that of the NIR driving pulse. The wavelength-selected XUV pulses are combined with a replica of the 795 nm NIR pulse using an annular mirror, and are focused into the interaction region of a velocity map imaging spectrometer (VMIS), which is capable of recording energy- and angle-resolved photoelectron spectra [36]. Both XUV and NIR beams are linearly polarized along the axis perpendicular to the symmetry axis of the VMIS spectrometer.

LAPE images are recorded using 29.6 eV photons (harmonic 19) at two different NIR peak intensities. The two images are recorded during the same experimental run within a short period of time ensuring that that the parameters of the laser system remain stable. We subtract weak contributions due to ionization by the NIR pulse alone and ensure that the XUV beam intensity and detection efficiency are the same (within 0.2%) for the two images by comparing the total photoelectron yield in the two measurements. The mode profile of the NIR laser beam in the focus, which is required for a calculation of the experimentally used laser intensities, cannot be measured directly in the present experiments. Therefore, the NIR intensity of about 5.9 TW/cm^2 is determined by comparing the overall shape of the measured spectra with the theoretical results of Sec. IV, while the ratio between the two employed intensities of 1.08 is determined by the ratio of the NIR pulse energies used in the experiment. The uncertainty of the pulse energy measurement is approximately 1%. VMIS records an Abel projection of the 3D photoelectron distributions, the 3D distributions are recovered by Abel inversion of the raw experimental images using the BASEX reconstruction algorithm [37]. Figs. 1 (a) and (b) show reconstructed 2D slices through the full 3D photoelectron distributions as false-color energy-angle maps. The photoelectron emission angle is relative to the laser polarization axis. The energy and angular resolution in the images is limited by the VMIS focusing optics: approximately 0.7 eV and 1.5°, respectively, in the region of the most intense signal. Both maps show sets of vertical lines corresponding to the main photoemission line (XUV-only) and a set of sidebands with lower and higher kinetic energies.

Many sidebands can be observed in these experiments, but no modulations (gross structure) are visible in the images, although previous calculations predict that at these laser fields the intracycle interference should play a role [17, 27–29, 38]. The absence of the gross structure in these measurements can be adjudicated to the averaging over a range of NIR intensities in the focal volume, varying from the maximum NIR intensity to almost zero across the focal volume [34]. Since the positions of angular features induced by intracycle interferences depend on the intensity of the NIR field, averaging over the experimental focus washes out these structures. We show the accuracy of this statement in Sec. IV with the aid of TDSE calculations.

To recover the gross structure we evaluate the difference between two angle-resolved photoelectron distributions recorded at the two slightly different NIR intensities of Fig. 1(a) and (b) in the spirit of the theory of the next section. The result after normalization of the individual measurements and subtraction is shown (as discussed in Sec. III, Eq. (9) in Fig. 1 (c) as a false-color map. Subtracting one image from the other reveals predominantly the contributions due to the highest NIR laser intensity and thus shows modulations in the emission angle corresponding to the intracycle interferences. This method appears to be very practical for observing gross struc-

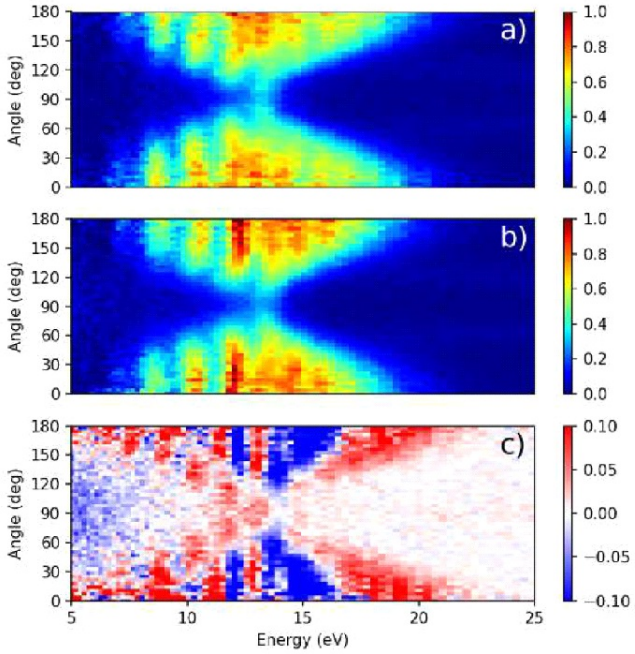

FIG. 1. Angle-resolved photoelectron spectra obtained in two-color XUV+NIR laser-assisted photoionization of argon. The argon atoms are ionized by 29.6 eV XUV photons (harmonic 19) in the presence of an 795 nm NIR laser field with intensities of a) 5.9 TW/cm^2, and b) 5.5 TW/cm^2. In (c) the difference between the two measurements shown in (a) and (b) is presented. Red colors indicate signal enhancement in the velocity map image taken at higher laser intensity, while blue colors indicate a reduction.

tures in laser-assisted photoemission in the common case of matched foci of the pump-probe XUV-NIR beams.

III. THEORY AND METHODS OF CALCULATION

The TDSE is solved in the SAE approximation with the Hamiltonian of the system described within the dipole approximation in the velocity gauge in the form [39]

$$H = \frac{\vec{p}^2}{2} + V(r) - \vec{p}\cdot\vec{A}(t) + \frac{\vec{A}^2(t)}{2}, \qquad (1)$$

where $\vec{p}$ is the electron momentum, $V(r)$ is a model potential describing the Coulomb interaction between the active electron and the core. The total vector potential $\vec{A}(t) = \vec{A}_{\rm NIR}(t) + \vec{A}_{\rm XUV}(t)$ is the sum of the vector potentials of the XUV and NIR pulses, obtained by $\vec{A}_{\rm XUV,NIR}(t) = -\int_{-\infty}^{t} \vec{F}_{\rm XUV,NIR}(t')dt'$.

The radial grid coordinate is discretized using 4000 points with a uniform grid step of $\Delta r = 0.05$ a.u.. In order to minimize unphysical reflections of the wave function at the boundary of the simulation box, a complex boundary absorber [40] is placed at a distance of 167.3 a_0 from the origin. The simulation includes angular momenta channels up to $L \leq 40, |M| \leq 40$. The time step is $\Delta t = 0.01$ a.u.. In order to calculate angle- and energy-resolved continuum photoelectron distributions the iSURFV [41] method is used, which extends to infinite time the surface flux method [42, 43].

The parameters of the long range potential $V(r)$ are chosen to reproduce the ionization potential $I_p = 15.76$ eV of argon and the energies of lower excited bound states [44]. Propagation of the wavefunction starts from the initial $3p$ ground state orbitals φ_{3pm}, where the magnetic quantum number $m = -1, 0$, or 1 describes the alignment of the $3p$-orbital with respect to the laser polarization axis. Our calculations show that the ionization of the different orbitals has similar total ionization probabilities and therefore all must be considered in the resulting spectrum.

Laser intensity variation over the focal volume implies variations of the LAPE spectra. Following the work of Posthumus for a single color laser [45, 46], we consider the laser propagation within the framework of Gaussian optics, where the intensity profile is characterized by a Lorentzian distribution along the laser propagation direction $\hat{\zeta}$ and by a Gaussian distribution along the radial direction $\hat{\rho}$, with cylindrical symmetry around the $\zeta-$axis. At $\zeta = \rho = 0$, the intensity of the XUV and NIR laser fields are $I_{\rm XUV,0}$ and $I_{\rm NIR,0}$, respectively. Away from the focus, the intensity distributions of the XUV and NIR laser beams thus decrease according to

$$I_{\rm XUV,NIR} = \frac{I_{\rm XUV,NIR,0}}{1+\left(\frac{\zeta}{\zeta_{\rm XUV,NIR}}\right)^2} \times \qquad (2)$$
$$\times \exp\left\{-\frac{2\rho^2}{\rho^2_{\rm XUV,NIR}\left[1+\left(\frac{\zeta}{\zeta_{\rm XUV,NIR}}\right)^2\right]}\right\},$$

where $\rho_{\rm XUV,NIR}$ is the waist at the focus, $\rho_{\rm XUV,NIR}\left[1+\left(\frac{\zeta}{\zeta_{\rm XUV,NIR}}\right)^2\right]$ describes the evolution of the waist along the propagation axis, and $\zeta_{\rm XUV,NIR}$ is the Rayleigh range of the XUV and NIR laser beams. The Rayleigh length $\zeta_{\rm XUV,NIR}$ can be calculated as $\zeta_{\rm XUV,NIR} = \pi\rho^2_{\rm XUV,NIR}/\lambda$ where λ is the wavelength of the corresponding laser, or equivalently

$$\zeta_{\rm XUV,NIR} = \frac{\rho^2_{\rm XUV,NIR}\,\omega_{\rm XUV,NIR}}{2c}. \qquad (3)$$

In Eq. (3) the Rayleigh length is proportional to the frequency $\omega_{\rm XUV,NIR}$, where c is the speed of light. The volume where ionization takes place is limited to the region of overlap of the argon jet and the laser beam, which we suppose is symmetric at the waist.

The average over the focal volume of the angle-resolved

photoelectron spectrum is defined as

$$\left\langle \frac{dP}{\sin\theta dE d\theta} \right\rangle = \frac{1}{V}\int \left(\frac{dP}{\sin\theta dE d\theta} \right) dV, \qquad (4)$$

where the $dP/(\sin\theta dE d\theta)$ in the right hand side of Eq. (4) is the electron emission distribution calculated for the respective XUV and NIR intensities $I_{\rm XUV}$ and $I_{\rm NIR}$, according to Eq. (2). Considering that for $|\zeta| < \zeta_{\rm jet}$ the gas density is constant, and for $|\zeta| > \zeta_{\rm jet}$ it is zero, Eq. (4) becomes

$$\left\langle \frac{dP}{\sin\theta dE d\theta} \right\rangle = \frac{2\pi}{V}\int_0^\infty d\rho\ \rho \int_{-\zeta_{\rm jet}}^{+\zeta_{\rm jet}} d\zeta \left(\frac{dP}{\sin\theta dE d\theta} \right). \qquad (5)$$

In order to calculate the volume average in Eq. (5), we must integrate over the variables ρ and ζ or, through the change of variables defined in Eq. (2), over the intensities $I_{\rm XUV}$ and $I_{\rm NIR}$. As the calculations of $dP/(\sin\theta dE d\theta)$ for a single intensity are a challenge by themselves, performing the average of Eq. (5) becomes computationally very expensive. For example, if we choose a grid of n points for each of both $I_{\rm XUV}$ and $I_{\rm NIR}$ variables, we would need n^2 calculations of the distribution for the n^2 pairs of intensities $(I_{\rm XUV}, I_{\rm NIR})$. In the following we show how to overcome this difficulty.

At the moderate laser intensities of the present experiment, the contributions from XUV+NIR ionization are well separated from the above threshold ionization yield resulting from the NIR pulse alone. Therefore, considering the first Born approximation for the ionization by one XUV photon, the ionization probability is proportional to the intensity of the XUV field, i.e., $P \propto I_{\rm XUV}(\zeta,\rho)$. Hence,

$$\left.\frac{dP}{\sin\theta dE d\theta}\right|_{I_{\rm XUV},I_{\rm NIR}} = \left(\frac{I_{\rm XUV}}{I_{\rm XUV,0}}\right) \left.\frac{dP}{\sin\theta dE d\theta}\right|_{I_{\rm XUV,0},I_{\rm NIR}}. \qquad (6)$$

and a grid in the XUV intensity is not needed within the TDSE calculations. Therefore, we only need to compute the angle- and energy-resolved photoelectron distributions for different values of $I_{\rm NIR}$.

For the special case of a narrow atomic jet, i.e., $\zeta_{\rm jet} \ll \zeta_{NIR} \ll \zeta_{XUV}$ [the second inequality is reasonably fulfilled due to $\omega_{XUV} \gg \omega_{NIR}$ in Eq. (3)], the laser intensity distribution near the focus as given by Eq. (2) can be approximated removing its ζ dependence as

$$I_{\rm XUV,NIR} = I_{\rm XUV,NIR,0} \exp\left(-\frac{2\rho^2}{\rho^2_{\rm XUV,NIR}}\right). \qquad (7)$$

From Eq. (7), it is easy to see that both the XUV and NIR laser intensities at the same radial position ρ must be related in the following way

$$\left(\frac{I_{\rm XUV}}{I_{\rm XUV,0}}\right)^{\rho^2_{\rm XUV}} = \left(\frac{I_{\rm NIR}}{I_{\rm NIR,0}}\right)^{\rho^2_{\rm NIR}}. \qquad (8)$$

Under these assumptions, each NIR intensity occurs in combination with only one specific XUV intensity. In our calculations, once we have chosen a grid of n points for the intensity $I_{\rm NIR}$ according to the NIR peak intensity in the experiment, the grid in $I_{\rm XUV}$ is directly determined by Eq. (8). Therefore, we only need n calculations of the electron distribution for the n pairs of intensities $(I_{{\rm NIR},i}, I_{{\rm XUV},i})$ with $(i = 0, ..., n)$.

Regarding Eq. (7), the incremental focal volume comprised between two radii ρ_1 and ρ_2, corresponding to two slightly different intensities $I_{\rm XUV,NIR,1}$ and $I_{\rm XUV,NIR,2}$ is given by [45] $\Delta V = \pi\ \zeta_{\rm jet}\rho^2_{\rm XUV}\log\left(\frac{I_{\rm XUV,1}}{I_{\rm XUV,2}}\right) = \pi\ \zeta_{\rm jet}\rho^2_{\rm NIR}\log\left(\frac{I_{\rm NIR,1}}{I_{\rm NIR,2}}\right)$. When we include the volume difference into the expression for the focal volume average [Eq. (5)], the average over the focal volume can be approximated to a discrete sum as

$$\left\langle \frac{dP}{\sin\theta dE d\theta} \right\rangle \simeq \sum_{i=1}^{n} w_i \left.\frac{dP}{\sin\theta dE d\theta}\right|_{I_{{\rm XUV},i},I_{{\rm NIR},i}}, \qquad (9)$$

where the weights are given by

$$w_i = \frac{\pi\zeta_{\rm jet}\rho^2_{\rm NIR}}{V}\log\left(\frac{I_{{\rm NIR},i}}{I_{{\rm NIR},i-1}}\right) \qquad (10a)$$

$$= \frac{\pi\zeta_{\rm jet}\rho^2_{\rm XUV}}{V}\log\left(\frac{I_{{\rm XUV},i}}{I_{{\rm XUV},i-1}}\right), \qquad (10b)$$

with $I_{{\rm NIR},i}$ and $I_{{\rm XUV},i}$ $(i = 0, ..., n)$ correspond to the intensity grid of the respective NIR and XUV laser pulses used in the TDSE calculations and the ionization distribution $dP/(\sin\theta dE d\theta)|_{I_{{\rm XUV},i},I_{{\rm NIR},i}}$ is calculated for a pair of intensities $(I_{{\rm XUV},i}, I_{{\rm NIR},i})$ linked between them through Eq. (8). It is precisely Eq. (8) which assures that the second right hand of Eq. (10a) is equal to the second right hand of Eq. (10b). According to Eq. (9) together with Eq. (10a) [Eq. (10b)], the evaluation of the difference between the average obtained for two slightly different peak intensities $I_{{\rm NIR},n}$ $(I_{{\rm XUV},n})$ and $I_{{\rm NIR},n-1}$ $(I_{{\rm XUV},n-1})$ results in the determination of the single intensity ionization probability $dP/\left(\sin\theta dE d\theta\right)|_{I_{{\rm XUV},i},I_{{\rm NIR},i}}$ up to the constant factor w_i. This factor can be approximated to $(\pi\zeta_{\rm jet}\rho^2_{\rm NIR}/V)(I_{{\rm NIR},n} - I_{{\rm NIR},n-1})/I_{{\rm NIR},n-1}$, or to $(\pi\zeta_{\rm jet}\rho^2_{\rm XUV}/V)(I_{{\rm XUV},n} - I_{{\rm XUV},n-1})/I_{{\rm XUV},n-1}$. In other words, the application of this substraction procedure (to the calculations or to the experimental data) allows to isolate the energy- and angle-resolved photoelectron distribution at the higher of the two peak intensities used.

For our experimental conditions in which the waist of the XUV and NIR laser pulses are roughly equal [34], i.e., $\rho_{\rm XUV} = \rho_{\rm NIR}$, Eq. (8) simplifies to a linear correlation,

$$\frac{I_{\rm XUV}}{I_{\rm XUV,0}} = \frac{I_{\rm NIR}}{I_{\rm NIR,0}}, \qquad (11)$$

which means that the ratios of intensities in Eq. (10a) for the NIR laser field and Eq. (10b) for the XUV laser field are the same [Eq. (11)].

IV. THEORETICAL RESULTS AND DISCUSSION

We now turn to calculating LAPE spectra for the laser field parameters used in the experiment. We consider a flat-top envelope for the NIR laser pulse to model long experimental fields in the calculations (this assumption has no significant influence on the results). The NIR laser field is thus written as

$$\vec{F}_{\rm NIR}(t) = F_{\rm NIR,0}(t)\ \cos\left[\omega_{\rm NIR}\left(t-\frac{\tau_{\rm NIR}}{2}\right)\right]\ \hat{z}, \quad (12)$$

with the envelope given by

$$F_{\rm NIR,0}(t) = F_{\rm NIR,0} \times \quad (13)$$
$$\times \begin{cases} \frac{\omega_{\rm NIR} t}{2\pi} & \text{if} \quad 0 \le t \le \frac{2\pi}{\omega_{\rm NIR}} \\ 1 & \text{if} \quad \frac{2\pi}{\omega_{\rm NIR}} \le t \le \tau_{\rm NIR} - \frac{2\pi}{\omega_{\rm NIR}} \\ \frac{(\tau_{\rm NIR}-t)\omega_{\rm NIR}}{2\pi} & \text{if} \quad \tau_{\rm NIR} - \frac{2\pi}{\omega_{\rm NIR}} \le t \le \tau_{\rm NIR} \end{cases}$$

and zero otherwise. This definition of the NIR pulse in Eqs. (12) and (14) assures a flat-top vector potential $A(t)$ fulfilling the boundary conditions $A(0) = A(\tau_{\rm NIR}) = 0$. We define the XUV pulse as a smooth sin-squared pulse between $t = \tau_{\rm NIR}/2 - \tau_{\rm XUV}/2$ and $\tau_{\rm NIR}/2 + \tau_{\rm XUV}/2$, i.e.,

$$\vec{F}_{\rm XUV}(t) = F_{\rm XUV,0}\ \sin^2\left[\frac{\pi}{\tau_{\rm XUV}}\left(t-\frac{\tau_{\rm NIR}-\tau_{\rm XUV}}{2}\right)\right]\times$$
$$\times\cos\left[\omega_{\rm XUV}\left(t-\frac{\tau_{\rm NIR}}{2}\right)\right]\ \hat{z}. \quad (14)$$

It is well known that the detailed XUV pulse shapes play a minor role in LAPE, especially for long NIR pulses [7, 10, 11]. For convenience, we consider an integer number of optical cycles in the XUV pulse, i.e., $N = \tau_{\rm XUV}\omega_{\rm XUV}/2\pi$.

We perform TDSE calculations for argon ionized by an XUV pulse of frequency $\omega_{\rm XUV} = 1.0925$ a.u. (29.73 eV), duration $\tau_{\rm XUV} = 5T_{\rm NIR} = 5 \times (2\pi/\omega_{\rm NIR}) = 546.4$ a.u. (13.22 fs) and an NIR laser pulse of frequency $\omega_{\rm NIR} = 0.0575$ a.u. (1.56 eV), and duration $\tau_{\rm NIR} = 7T_{\rm NIR} = 764.9$ a.u. (18.5 fs). Of the two different structures in LAPE, the sidebands stemming from the intercycle are robust enough to survive the intensity averaging of the different laser intensities into the focal volume, however, the gross structures stemming from intracycle interference are not. Intracycle emission takes place within one optical cycle and it is inherently independent of the pulse duration, as long as there are enough optical cycles in the pulse. For our calculations, we observe that a laser pulse of five optical cycles of duration is enough to reach the limit of long pulses and, therefore, can reproduce the experimental results. In Ref. [29] we showed the lack of dependence of the intracycle interference pattern with respect to the duration of the XUV pulse. We consider the argon atom initially in its ground $3p$ state ($I_p \simeq 0.58$ a.u. $= 15.8$ eV) and calculate angle- and energy-resolved distributions for photoelectrons with magnetic quantum numbers $m = 0, \pm 1$, defining the projections of the angular momentum along the polarization axis. Note that for symmetry reasons the calculation for $m = +1$ gives the same angle- and energy-resolved photoelectron distribution as a calculation for $m = -1$. The results of the calculations are shown in Fig. 2 for an NIR peak field $F_{\rm NIR,0} = 0.013$ a.u. ($I_{\rm NIR} = 5.9 \times 10^{12}$ W/cm^2). Due to the linear dependence of the electron yield on the XUV pulse intensity, we have arbitrarily chosen $F_{\rm XUV,0} = 0.0065$ a.u. ($I_{XUV} = 1.485 \times 10^{12}$ W/cm^2). In Fig. 2 (a), calculated for photoelectrons with $m = 0$, we observe that the electron emission is peaked along the polarization axis, i.e. at $\theta = 0°$ and 180°. Instead, in Fig. 2 (b) for ionization with $m = 1$, selection rules prohibit emission along the polarization axis enhancing, thus, the perpendicular emission [47]. The classical boundaries of

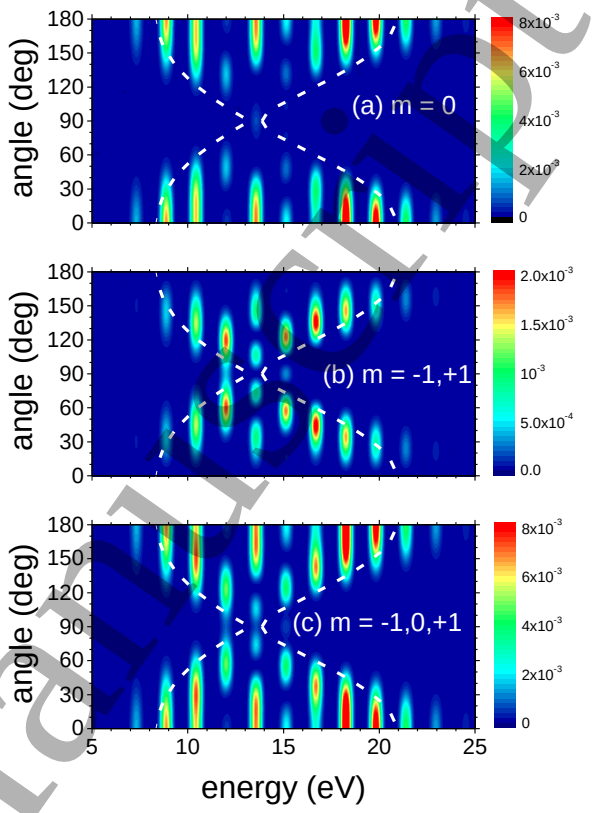

FIG. 2. Angle- and energy-resolved probability distribution for the ionization of Ar subject to an XUV pulse with $\omega_{\rm XUV} = 1.0925$ a.u. (29.7 eV), duration $\tau_{\rm XUV} = 5T_{\rm NIR}$ and an NIR laser pulse with a frequency $\omega_{\rm NIR} = 0.0575$ a.u. (1.56 eV), duration $\tau_{\rm NIR} = 7T_{\rm NIR}$, as calculated by solving the TDSE. The NIR laser peak field is $F_{\rm NIR,0} = 0.013$ a.u. ($I_{\rm NIR} = 5.9 \times 10^{12}$ W/cm^2). (a) Result for photoelectrons with magnetic quantum number $m = 0$, (b) result for $m = \pm 1$, and (c) sum of the distributions for $m = -1, 0, +1$. Classical boundaries [29] are indicated by dashed lines.

the electron distributions according to Refs. [27–29] are shown in dashed lines in Fig. 2. For emission parallel to both polarization axis the classically allowed region is limited to

$$\frac{(v_0 - F_{\mathrm{NIR},0}/\omega_{\mathrm{NIR}})^2}{2} < E < \frac{(v_0 + F_{\mathrm{NIR},0}/\omega_{\mathrm{NIR}})^2}{2}, \tag{15}$$

where $v_0^2/2 = \omega_{\mathrm{XUV}} - I_p$ corresponds to the electron kinetic energy for ionization by the XUV pulse only [27]. In the perpendicular direction the electron kinetic energy is classically restricted to [28]

$$\frac{\left[v_0^2 - (F_{\mathrm{NIR},0}/\omega_{\mathrm{NIR}})^2\right]}{2} < E < \frac{v_0^2}{2}. \tag{16}$$

For argon ionization by the laser fields described above ($v_0^2/2 = 0.51$ a.u. $= 13.9$ eV) the energy domain is classically limited to 0.309 a.u. (8.41 eV) $< E <$ 0.767 a.u. (20.87 eV) along the polarization axis and to 0.487 a.u. (13.25 eV) $< E <$ 0.51 a.u. (13.9 eV) in the perpendicular direction. The calculated distributions extend beyond these classical boundaries due to the quantum nature of the final wave function.

The vertical iso-energy stripes in Fig. 2 correspond to sidebands arising from the absorption of an XUV photon accompanied by the absorption (emission) of a positive (negative) integer number n of NIR photons in agreement with the conservation of energy

$$E_n = n\omega_{\mathrm{NIR}} + \omega_{\mathrm{XUV}} - I_p - U_p. \tag{17}$$

Eq. (17) expresses that the energy of all photoelectron peaks (i.e. both the XUV mainline and all sidebands) are shifted down by the ponderomotive energy of the NIR laser $U_p = (F_{\mathrm{NIR},0}/2\omega_{\mathrm{NIR}})^2 = 0.0128$ a.u. (0.348 eV). *Odd* sidebands arise as a result of the absorption of an *even* number of photons (one XUV photon and an odd number of NIR photons). For perpendicular emission ($\theta = 90°$), the odd sidebands are missing for ionization with the magnetic quantum number $m = 0$ due to the selection rule for angular momentum, or equivalently, as a result of the destructive interhalfcycle interference, thus we can see the zero order sideband in Fig. 2 (a) [28, 47]. Instead, for ionization with $m = \pm 1$ even sidebands are missing as a result of the selection rule for angular momentum [47], thus Fig. 2 (b) exhibits no zero-order sideband, and the first order sidebands are clearly visible for perpendicular emission (at both sides of the main ionization line) at $E \simeq 13.5$ eV .

We can observe in Fig. 2 that the sidebands display an angle-dependent modulation which stems from intracycle interference (see [27–29]). There is a very good resemblance of the TDSE distribution of Fig. 2 (a) to the semiclassical (strong field) results in Ref. [29], which indicates a minor role of the Coulomb potential in the photoionization process [48]. In Fig. 2 (c) we have equiprobably summed up the contributions of the three possible projections of the angular momentum i.e., $m = 0, \pm 1$. The resulting angle- and energy-dependent photoelectron distribution differs significantly from both the m=0 calculation and the $m = \pm 1$ calculation, illustrating that both must be taken into account in order to properly describe the experiment.

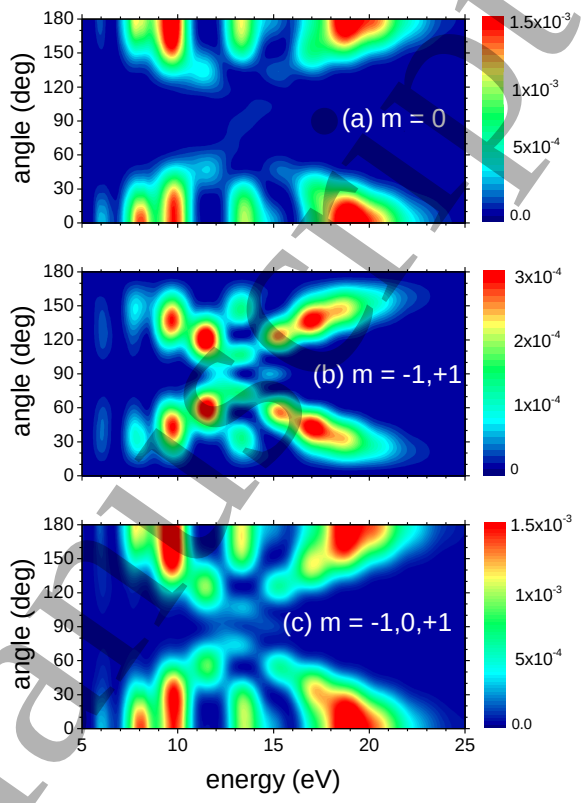

FIG. 3. Angle- and energy-resolved probability distribution for the ionization of Ar subject to a flat-top XUV pulse of $\omega_{\mathrm{XUV}} = 1.0925$ a.u. (29.73 eV), duration $\tau_{\mathrm{XUV}} = T_{\mathrm{NIR}}$ and an NIR laser pulse with a frequency $\omega_{\mathrm{NIR}} = 0.0575$ a.u. (1.56 eV) and duration $\tau_{\mathrm{NIR}} = 7T_{\mathrm{NIR}}$. The NIR laser peak field is $F_{\mathrm{NIR},0} = 0.013$ ($I_{\mathrm{NIR}} = 5.9 \times 10^{12}$ W/cm^2) (a) corresponds to $m = 0$, (b) to $m = \pm 1$, and (c) to the sum of the three distributions for $m = -1, 0, +1$.

In order to illustrate that the angular structure of the sidebands in Fig. 2 stems from intracycle interference of electron trajectories released within the same optical laser cycle, we have performed calculations for an XUV pulse duration of only one optical cycle, i.e. $\tau_{\mathrm{XUV}} = T_{\mathrm{NIR}} = (2\pi/\omega_{\mathrm{NIR}}) = 109.3$ a.u. (2.64 fs) considering a flat-top envelope of the XUV pulse instead of the sin-squared envelope in Eq. (14). In Fig. 3 we observe that as ionization takes place essentially within a single cycle of the NIR field, no sidebands resulting from intercycle interferences are formed, and only the intracycle

interference structures remain visible in the maps. The angular modulations of the sidebands, which stem from the intracycle interference for the five-cycle XUV pulse in Fig. 2 look essentially the same as those arising from intracycle interference (for $\tau_{\rm XUV} = T_{\rm NIR}$ calculation) in Fig. 3. Semiclassical calculations in Ref. [29] exclude interferences between contributions from the ground state and from excited states (releasing their wave packets at the same initial time) since those calculations considers only one bound state. Therefore, the agreement between the current TDSE results and the semiclassical calculations in Ref. [29] leads us to the conclusion that intracycle interferences are the only source of the gross structure.

As discussed in Sec. II, if we want to compare our simulations with the experiment, we need to average the electron spectra over the experimental intensity distribution in the focal volume (see Sec. III) and consider a random orientation of the angular momentum. We assume that both the NIR and the XUV beams have Gaussian profiles with a waist radius $\rho_{\rm XUV} = \rho_{\rm NIR} = w = 0.1$ mm. For the XUV beam this waist radius corresponds to a Rayleigh length of $\zeta_{\rm XUV} = 190$ mm and for the NIR beam the Rayleigh length is $\zeta_{\rm NIR} = 10$ mm. In Fig. 4 (a) we present the result of averaging the distributions calculated by solving the TDSE over the focal volume according to Eq. (9) for an XUV peak field at the focus of $F_{\rm XUV,0} = 0.0065$ and an NIR laser peak field at the focus of $F_{\rm NIR,0} = 0.013$ ($I_{\rm NIR} = 5.9 \times 10^{12}$ W/cm^2). The NIR and XUV frequencies and laser pulse durations are the same as in Fig. 2. The general features of the distribution are similar to the non-averaged distributions in Fig. 2 (c) except for the vanishing of the intracycle interference pattern. This disappearence of the intracycle interference pattern agrees with the experimental observations [see Fig. 1 (a) and (b)]. For the sake of comparison, we have smoothened the angle- and energy-resolved probability distribution in Fig. 4 (a) using an energy window of about 0.9 eV and an angular window of about 1° similar to the experimental resolution described in Sec. II. To the extent that the remaining features permit such a comparison, the resulting smoothed distribution of Fig. 4 (b) exhibits a good agreement with the experimental distribution in Fig. 1 (a). In Fig. 4 (a) and (b) we observe that the probability distribution in the direction parallel to both polarization axis extends from about 6 to 25 eV, very similar to the experimental data in Fig. 1 (a) and (b). Besides, for emission perpendicular to both polarization axis, the maximum lies at about 14 eV in the calculations [in Fig. 4 (a) and (b)] and the measurements [in Fig. 1 (a) and (b)].

In order to recover the intracycle interference pattern, we repeat the procedure performed for the experimental data and calculate photoelectron distributions for two different NIR laser peak fields $F_{\rm NIR,0} = 0.013$ and $F_{\rm NIR,0} = 0.0125$ (intensities of 5.9×10^{12} W/cm^2 and 5.5×10^{12} W/cm^2, respectively). Similar to the analysis of the experimental data in Section II, we normalize the two calculated electron energy- and angular distributions before subtracting by using Eq. (9). Fig. 4 (c) shows the resulting difference maps for the TDSE calculations. To account for the experimental resolution we again smoothen the calculated maps in Fig. 4 (d), whose intracycle structure pattern can be immediately identified, despite not being visible in Fig. 4 (a) and (b). There is a strong similarity between the pattern of Fig. 4 (d) and that of Fig. 3 (c) confirming that the subtraction procedure indeed gives access to the gross structure,

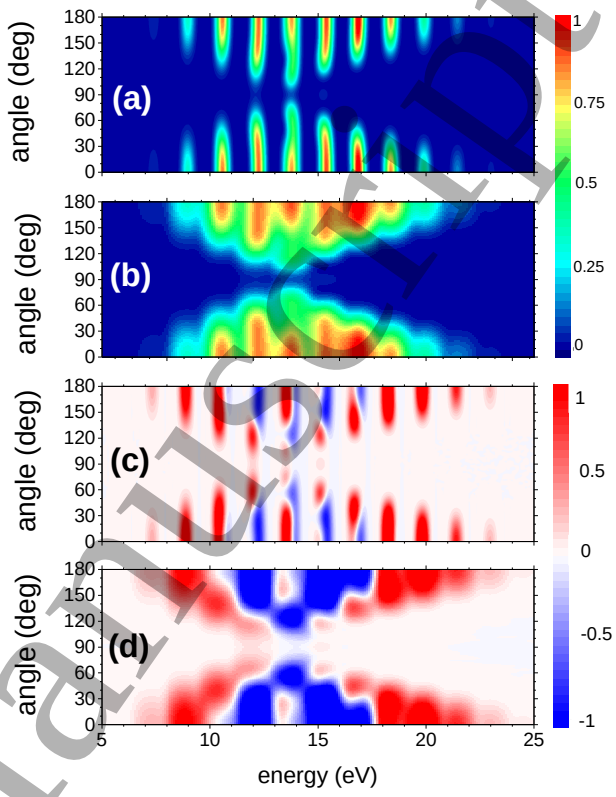

FIG. 4. TDSE angle- and energy-resolved probability distribution for the ionization of Ar subject to an XUV pulse with $\omega_{\rm XUV} = 1.0925$ a.u. (29.73 eV), duration $\tau_{\rm XUV} = 5T_{\rm NIR}$ and an NIR laser pulse with a frequency $\omega_{\rm NIR} = 0.0575$ a.u. (1.56 eV), duration $\tau_{\rm NIR} = 7T_{\rm NIR}$ and peak field $F_{\rm NIR,0} = 0.013$ a.u. ($I_{\rm NIR} = 5.9 \times 10^{12}$ W/cm^2). (a) corresponds to calculations averaged over the focal volume [Eq. (5)]. (b) idem (a) where the distribution was smoothened using an energy window of about 0.9 eV and an angle window of about 1° to account for the experimental resolution. (b) idem (a) but (c) corresponds to the difference between the normalized distributions calculated in (a) and the corresponding to a NIR laser peak field $F_{\rm NIR,0} = 0.0125$ a.u. ($I_{\rm NIR} = 5.5 \times 10^{12}$ W/cm^2), (not shown). (d) is the same as (c) but smoothened in the same way as (b). All intensities are in arbitrary units and plotted in a linear scale.

which is otherwise washed out by averaging over the NIR intensity distribution in the focus. The difference maps are also in very good agreement with the experimental data in Fig. 1(c). Summing up, the intracycle interference appearing in LAPE at sufficiently high NIR laser intensities can be reliably recovered by subtracting distributions recorded at two slightly different NIR laser fields, even when these interferences are washed out by variations of the NIR laser intensity in the focus. It is worth to mention that, due to the normalization of the two probability distributions averaged over the focal volume, the resulting difference distributions in Fig. 4 (c) and (d) are not probability distributions since its integral in energy and angle is thus zero.

V. CONCLUSIONS

We performed experiments on laser-assisted XUV ionization of argon atoms and recorded energy- and angle-resolved photoelectron spectra. The sidebands due to the intercycle interference survive the averaging over the focal volume because of the small value of the ponderomotive energy at peak NIR intensity compared to the NIR photon energy. In contrast, we observe that the intracycle interference pattern is completely washed out and cannot be directly observed in the experimental data due to averaging over the focal volume. However, by subtracting two photoelectron distributions for slightly different NIR peak laser intensities the intracycle interference pattern is recovered. We performed full TDSE calculations for pairs of NIR and XUV peak intensities, averaged the resulting distributions over the focal volume of both laser pulses and compared the differential angle-energy maps with the experimental results. Under the assumption of a homogeneous gas density, the theory supports the subtraction procedure as a reliable tool to recover intracycle interference in LAPE. In doing so, we showed for the photoelectrons emitted from the $3p$ orbital of argon the relevance of the three possible projections of the angular momentum on the laser polarization axis $m = 0, \pm 1$. The high degree of resemblance between the TDSE results and the experiment confirms that the subtraction procedure can be used to unravel the intracycle gross structure in photoelectron spectra, despite being washed out by the spatial variation of the NIR laser intensity in the focus.

ACKNOWLEDGMENTS

We are grateful to N. Kabachnik for fruitful discussions and early support. Work supported by bilateral Argentine-German grant CONICET-DAAD of 2015, the grant of Deutsche Forschungsgemeinschaft (KO 4920/1-1), and by CONICET PIP0386, PICT-2016-0296 and PICT-2017-2945 of ANPCyT (Argentina).

[1] V. Véniard, R. Taïeb, and A. Maquet, Physical Review Letters **74**, 4161 (1995).
[2] J. M. Schins, P. Breger, P. Agostini, R. C. Constantinescu, H. G. Muller, A. Bouhal, G. Grillon, A. Antonetti, and A. Mysyrowicz, J. Opt. Soc. Am. B **13**, 197 (1996).
[3] T. E. Glover, R. W. Schoenlein, A. H. Chin, and C. V. Shank, Physical Review Letters **76**, 2468 (1996).
[4] J. Itatani, F. Quéré, G. L. Yudin, M. Y. Ivanov, F. Krausz, and P. B. Corkum, Phys. Rev. Lett. **88**, 173903 (2002).
[5] U. Frühling, M. Wieland, M. Gensch, T. Gebert, B. Schutte, M. Krikunova, R. Kalms, F. Budzyn, O. Grimm, J. Rossbach, E. Plonjes, and M. Drescher, Nat Photon **3**, 523 (2009).
[6] M. Wickenhauser, J. Burgdörfer, F. Krausz, and M. Drescher, Journal of Modern Optics **53**, 247 (2006), http://dx.doi.org/10.1080/09500340500259870.
[7] S. Düsterer, L. Rading, P. Johnsson, A. Rouzée, A. Hundertmark, M. J. J. Vrakking, P. Radcliffe, M. Meyer, A. K. Kazansky, and N. M. Kabachnik, Journal of Physics B: Atomic, Molecular and Optical Physics **46**, 164026 (2013).
[8] S. Düsterer, G. Hartmann, F. Babies, A. Beckmann, G. Brenner, J. Buck, J. Costello, L. Dammann, A. De Fanis, P. Geßler, L. Glaser, M. Ilchen, P. Johnsson, A. K. Kazansky, T. J. Kelly, T. Mazza, M. Meyer, V. L. Nosik, I. P. Sazhina, F. Scholz, J. Seltmann, H. Sotoudi, J. Viefhaus, and N. M. Kabachnik, Journal of Physics B Atomic Molecular Physics **49**, 165003 (2016).
[9] S. Minemoto, H. Shimada, K. Komatsu, W. Komatsubara, T. Majima, T. Mizuno, S. Owada, H. Sakai, T. Togashi, S. Yoshida, M. Yabashi, and A. Yagishita, Journal of Physics B Atomic Molecular Physics **51**, 075601 (2018).
[10] M. Meyer, J. T. Costello, S. Düsterer, W. B. Li, and P. Radcliffe, Journal of Physics B Atomic Molecular Physics **43**, 194006 (2010).
[11] M. Meyer, P. Radcliffe, T. Tschentscher, J. T. Costello, A. L. Cavalieri, I. Grguras, A. R. Maier, R. Kienberger, J. Bozek, C. Bostedt, S. Schorb, R. Coffee, M. Messerschmidt, C. Roedig, E. Sistrunk, L. F. di Mauro, G. Doumy, K. Ueda, S. Wada, S. Düsterer, A. K. Kazansky, and N. M. Kabachnik, Physical Review Letters **108**, 063007 (2012).
[12] M. Drescher and F. Krausz, Journal of Physics B: Atomic, Molecular and Optical Physics **38**, S727 (2005).
[13] E. Goulielmakis, M. Uiberacker, R. Kienberger, A. Baltuska, V. Yakovlev, A. Scrinzi, T. Westerwalbesloh, U. Kleineberg, U. Heinzmann, M. Drescher, and F. Krausz, Science **305**, 1267 (2004), http://science.sciencemag.org/content/305/5688/1267.full.pdf.
[14] P. Johnsson, R. López-Martens, S. Kazamias, J. Mauritsson, C. Valentin, T. Remetter, K. Varjú, M. B. Gaarde, Y. Mairesse, H. Wabnitz, P. Salières, P. Balcou, K. J. Schafer, and A. L'Huillier, Phys. Rev. Lett. **95**, 013001 (2005).

[15] A. K. Kazansky and N. M. Kabachnik, Journal of Physics B: Atomic, Molecular and Optical Physics **43**, 035601 (2010).
[16] A. K. Kazansky, I. P. Sazhina, and N. M. Kabachnik, Phys. Rev. A **82**, 033420 (2010).
[17] S. Bivona, G. Bonanno, R. Burlon, and C. Leone, Laser Physics **20**, 2036 (2010).
[18] P. Radcliffe, M. Arbeiter, W. B. Li, S. Düsterer, H. Redlin, P. Hayden, P. Hough, V. Richardson, J. T. Costello, T. Fennel, and M. Meyer, New Journal of Physics **14**, 043008 (2012).
[19] A. Maquet and R. Taïeb, Journal of Modern Optics **54**, 1847 (2007), http://dx.doi.org/10.1080/09500340701306751.
[20] M. J. Nandor, M. A. Walker, L. D. Van Woerkom, and H. G. Muller, Phys. Rev. A **60**, R1771 (1999).
[21] H. G. Muller, Phys. Rev. A **60**, 1341 (1999).
[22] A. Jiménez-Galán, L. Argenti, and F. Martín, New Journal of Physics **15**, 113009 (2013).
[23] M. Meyer, D. Cubaynes, P. O'Keeffe, H. Luna, P. Yeates, E. T. Kennedy, J. T. Costello, P. Orr, R. Taïeb, A. Maquet, S. Düsterer, P. Radcliffe, H. Redlin, A. Azima, E. Plönjes, and J. Feldhaus, Phys. Rev. A **74**, 011401 (2006).
[24] M. Meyer, D. Cubaynes, D. Glijer, J. Dardis, P. Hayden, P. Hough, V. Richardson, E. T. Kennedy, J. T. Costello, P. Radcliffe, S. Düsterer, A. Azima, W. B. Li, H. Redlin, J. Feldhaus, R. Taïeb, A. Maquet, A. N. Grum-Grzhimailo, E. V. Gryzlova, and S. I. Strakhova, Physical Review Letters **101**, 193002 (2008).
[25] P. O'Keeffe, R. López-Martens, J. Mauritsson, A. Johansson, A. L'Huillier, V. Véniard, R. Taïeb, A. Maquet, and M. Meyer, Phys. Rev. A **69**, 051401 (2004).
[26] P. Hayden, J. Dardis, P. Hough, V. Richardson, E. T. Kennedy, J. T. Costello, S. Düsterer, H. Redlin, J. Feldhaus, W. B. Li, D. Cubaynes, and M. Meyer, Journal of Modern Optics **63**, 358 (2016), http://dx.doi.org/10.1080/09500340.2015.1117669.
[27] A. A. Gramajo, R. Della Picca, C. R. Garibotti, and D. G. Arbó, Physical Review A **94**, 053404 (2016), arXiv:1605.07457 [physics.atom-ph].
[28] A. A. Gramajo, R. Della Picca, and D. G. Arbó, Physical Review A **96**, 023414 (2017), arXiv:1703.09585 [physics.atom-ph].
[29] A. A. Gramajo, R. Della Picca, S. D. López, and D. G. Arbó, Journal of Physics B Atomic Molecular Physics **51**, 055603 (2018).
[30] M. Eckstein, C.-H. Yang, M. Kubin, F. Frassetto, L. Poletto, H.-H. Ritze, M. J. J. Vrakking, and O. Kornilov, The Journal of Physical Chemistry Letters **6**, 419 (2015), pMID: 26261958, https://doi.org/10.1021/jz5025542.
[31] V. Véniard, R. Taïeb, and A. Maquet, Phys. Rev. A **54**, 721 (1996).
[32] P. M. Paul, E. S. Toma, P. Breger, G. Mullot, F. Augé, P. Balcou, H. G. Muller, and P. Agostini, Science **292**, 1689 (2001), https://science.sciencemag.org/content/292/5522/1689.full.pdf.
[33] A. T. J. B. Eppink and D. H. Parker, Review of Scientific Instruments **68**, 3477 (1997).
[34] M. Kubin, Master's Thesis, Freie Universität Berlin, Berlin (2013).
[35] M. Eckstein, J. Hummert, M. Kubin, C.-H. Yang, F. Frassetto, L. Poletto, M. J. Vrakking, and O. Kornilov, arXiv preprint arXiv:1604.02650 (2016).
[36] O. Ghafur, W. Siu, P. Johnsson, M. F. Kling, M. Drescher, and M. J. J. Vrakking, Rev. Sci. Instrum. **80**, 033110 (2009).
[37] V. Dribinski, A. Ossadtchi, V. A. Mandelshtam, and H. Reisler, Review of Scientific Instruments **73**, 2634 (2002).
[38] A. K. Kazansky and N. M. Kabachnik, Journal of Physics B: Atomic, Molecular and Optical Physics **39**, 5173 (2006).
[39] S. Patchkovskii and H. Muller, Computer Physics Communications **199**, 153 (2016).
[40] D. E. Manolopoulos, The Journal of Chemical Physics **117**, 9552 (2002), https://doi.org/10.1063/1.1517042.
[41] F. Morales, T. Bredtmann, and S. Patchkovskii, Journal of Physics B: Atomic, Molecular and Optical Physics **49**, 245001 (2016).
[42] A. M. Ermolaev, I. V. Puzynin, A. V. Selin, and S. I. Vinitsky, Phys. Rev. A **60**, 4831 (1999).
[43] L. Tao and A. Scrinzi, New Journal of Physics **14**, 013021 (2012).
[44] H. G. Muller and F. C. Kooiman, Physical Review Letters **81**, 1207 (1998).
[45] J. Posthumus, *Molecules and Clusters in Intense Laser Fields, Cambridge, UK: Cambridge University Press* (2009).
[46] S. Augst, D. D. Meyerhofer, D. Strickland, and S. L. Chin, Journal of the Optical Society of America B Optical Physics **8**, 858 (1991).
[47] R. Della Picca, A. A. Gramajo, S. D. López, and D. G. Arbó, J. Phys. Conf. Series (2020), in press.
[48] D. G. Arbó, K. L. Ishikawa, K. Schiessl, E. Persson, and J. Burgdörfer, Phys. Rev. A **82**, 043426 (2010).